Molecular Fe-N_4 Moieties Coupled with Atomic Co-N_4 Sites towards Improved Oxygen Reduction Performance

Peng-Fei Xie[1], Hong Zhong[2], Lingzhe Fang[3], Zhaoyuan Lyu[2], Wan-Jing Yu[4], Tao Li[3, 5], Jiyoung Lee[6], Hamin Shin[7], Scott P. Beckman[2], Yuehe Lin[2], Shichao Ding[2], Il-Doo Kim[7],* Jin-Cheng Li[1,*]*

[1]Faculty of Chemical Engineering, Yunnan Provincial Key Laboratory of Energy Saving in Phosphorus Chemical Engineering and New Phosphorus Materials, Kunming University of Science and Technology, Kunming 650500, China.

[2]School of Mechanical and Materials Engineering, Washington State University, Pullman, WA 99164, United States.

[3]Department of Chemistry and Biochemistry, Northern Illinois University, 1425 W. Lincoln Hwy., DeKalb, IL, 60115, United States.

[4]School of Metallurgy and Environment, Central South University, Changsha 410083, China.

[5]X-ray Science Division, Argonne National Laboratory, 9700 South Cass Avenue, Lemont, Illinois 60439, United States.

[6]Department of Chemistry, Northwestern University, Evanston, IL 60208, USA.

[7]Department of Materials Science and Engineering, Korea Advanced Institute of Science and Technology, Daejeon 34141, Republic of Korea

Email: shichao.ding@wsu.edu; idkim@kaist.ac.kr; jinchengli@kust.edu.cn

KEYWORDS: CoSAC, iron phthalocyanine, density functional theory, oxygen reduction

Abstract:

Research on high-efficiency and cost-efficient catalysts for oxygen reduction reaction (ORR) is still a vital but challenging issue for commercializing fuel cells and metal-air batteries. Herein, a single-molecule/atom hybrid catalyst is developed to boost the ORR, in which iron phthalocyanine molecules containing molecular Fe-N_4 moieties couple with atomic Co-N_4 sites on the surface of polyhedral carbon. Density functional theory calculations reveal that face-to-face laminated construction of Fe-N_4 and Co-N_4 in the hybrid catalyst can effectively modulate the electronic structure of active iron atoms and reduce the energy barrier of the rate-determining step for ORR. As a result, this hybrid catalyst demonstrates excellent ORR performance, featuring a half-wave potential of 0.904 V, a peak power density of 238.3 mW cm^{-2} for zinc-air battery, and outstanding electrocatalytic stability. This work offers a distinctive and robust molecular/atomic engineering approach to creating efficient electrocatalysts, advancing the fields of fuel cells and metal-air batteries.

1. Introduction

As a critical bottleneck in developing fuel cells and metal-air batteries, sluggish oxygen reduction reaction (ORR) has recently inspired a new wave of research.[1] To expedite the notably sluggish kinetics, highly efficient catalysts are imperative to achieve the desired energy device performance.[2] Pt-based catalysts are optimal for the ORR but present drawbacks, including high cost and limited stability.[3] Extensive research is concentrated on cost-efficient Pt-free catalysts, primarily encompassing metal-free heteroatom-doped nanocarbons, carbon complexes anchored with Me-N_4 (Me = Fe, Co, Ni, and other transition metals) macrocycles, and noble-metal-free Me-N co-doped carbon (Me-N-C) nanomaterials.[4] The latter two classes contain atomically dispersed

Me active sites coordinated by N atoms. Such single-atom Me sites, especially in Fe sites with appropriate coordination environments, show a comparable ORR activity to Pt in theory.[5] Thus, much experimental research has been devoted to consciously adjusting the coordination environments, mainly including coordination numbers and coordinating heteroatoms, for substantial improvements in catalytic performances.[6]

Up to now, the universal strategy to realize the modulation of coordination environments around isolated Me atoms involves high-temperature pyrolysis of the precursors containing C, N, Me, and/or extra heteroatoms (in cases where coordination heteroatoms are present).[7] Heteroatoms may substitute the sites of N atoms (and/or C atoms) to occupy the first (and/or second) coordination shell of Me, or other molecular structures of atomic Me-N_x sites are preferentially formed using rational design of the precursors and pyrolysis parameters.[8] Such a strategy can modulate the electronic structure and enhance the ORR activity. However, the coordination structures of isolated Me atoms in the final materials are undefined and controversial due to the limitation of the high-temperature preparation method and characterization technique.[9] For example, our group developed a phosphorus doping of single-atom Fe-N-C nanowires in the presence of phytic acid.[10] Utilizing the current advanced characterization techniques such as X-ray absorption spectroscopy (XAS) and aberration-corrected transmission electron microscopy (TEM) together with density functional theory (DFT) calculations, a catalytic mechanism that a phosphorus atom occupying the second coordination shell of Fe boosts the ORR activity was proposed. Similarly, Yuan et al. employed this method to prepare atomically dispersed phosphorus-doped Fe-N-C catalysts.[11] However, by combining advanced characterization results with density functional theory calculations, they hypothesized that phosphorus might serve as the primary coordination atom. Notably, the assembly of heteroatom doping around atomic Me sites

is relatively random. A certain molecular structure of heteroatom doping around atomic Me sites can be preferentially generated by optimizing the pyrolysis conditions. Nevertheless, this synthetic method still challenges demonstrating molecular structures, potentially leading to an ambiguous structure-activity relationship of Me-N-C.[12]

Macrocycle molecule electrocatalyst can provide a relatively straightforward structure-activity relationship since the molecular structure is well-defined.[13-15] A series of molecule catalysts with defined Me-N_4 and Me-N_3C structures were developed by Huang et al. to reveal the electrocatalytic mechanisms for ORR.[14a] To enhance the electrocatalytic performance, macrocycle molecules are usually anchored onto highly graphitized surfaces through of $\pi-\pi$ coupling interaction at room temperature.[16-18] Based on this principle, many coupling hybrids have been developed. For instance, Chen et al. found that oxygen-doped graphene coupled with iron phthalocyanine (FePc) exhibits much improved ORR performance compared to its pure graphene-based counterpart.[19] Therein, oxygen is used as the coordination atom at the axial direction of Fe-N_4 in the planar FePc molecule. Cao et al. compared FePc anchored on carbon nanotube (CNT) with FePc stabilized on N-modified CNT, demonstrating that N acted as an axial ligand atom that can significantly boost the ORR activity.[20] Yu et al. hypothesized that defect graphene could efficiently modulate charge redistribution of atomic Fe-N_4 moiety in FePc, consequently leading to enhanced ORR activity.[21] These results demonstrate that modifying carbon substrates is an efficient strategy to adjust the coordination environments and achieve a substantial performance improvement.[22] However, the current research is limited to metal-free carbon substrates.

Herein, we develop a new class of coupling hybrid, where Me-N_4 macrocycle molecules are anchored onto carbon-based single-atom catalysts. As proof, FePc containing Fe-N_4 moieties is coupled with a single-atom Co catalyst (CoSAC) featuring Co-N_4 sites, resulting in a face-to-face

laminated arrangement of Fe-N_4 and Co-N_4 within the hybrid catalyst (denoted as CoSAC@FePc). The Fe active centers in CoSAC@FePc coordinate with four planar N atoms and one axial Co atom, which is revealed by aberration-corrected HAADF-STEM imaging and X-ray absorption spectroscopy analysis. Theoretical calculations and experimental studies verify that these Fe active centers in face-to-face Fe-N_4/Co-N_4 sites reduce the energy barrier of the rate-determining step for ORR, resulting in exceptional ORR performance. Finally, both liquid-state and solid-state zin-air batteries (ZABs) assembled using CoSAC@FePc demonstrate remarkably improved battery performance and practicality.

2. Results and Discussion

2.1 Structural characterizations

The synthetic process of CoSAC@FePc is illustrated in **Figure 1**a, involving ion exchange, pyrolysis, and coupling procedures of a metal-organic framework. Typically, Zn-based zeolitic-imidazolate-framework (ZIF-8) polyhedrons (Figure S1, Supporting Information) containing numerous Zn-N_4 units were prepared through a self-assembly reaction between Zn^{2+} and 2-methylimidazole. Subsequently, Co^{2+} was introduced to realize the ion exchange, in which some Zn atoms on the surface of ZIF-8 were substituted by Co atoms, forming Co-modified ZIF-8 (Co-ZIF-8).[23] The morphology of Co-ZIF-8 remains unchanged after the ion exchange, still presenting a polyhedral structure (Figure S2, Supporting Information). The Co-ZIF-8 precursor was pyrolyzed to achieve single-atom Co-N-doped carbon (CoSAC), which inherits the polyhedral structure (Figure S3, Supporting Information). Finally, the pyrolyzed CoSAC sample was used as a substrate to support FePc molecules through a simple sonicate-assisted coupling interaction. The resultant composite material was denoted as CoSAC@FePc. This coupling process has little impact on the morphology and structure. As shown in Figure 1b, polyhedral nanoparticles are

present in CoSAC@FePc. Besides, control samples of N-doped carbon (NC) without CoSAC and its coupling hybrid (NC@FePc) were synthesized, also showing a polyhedral structure (Figure S4, Supporting Information).

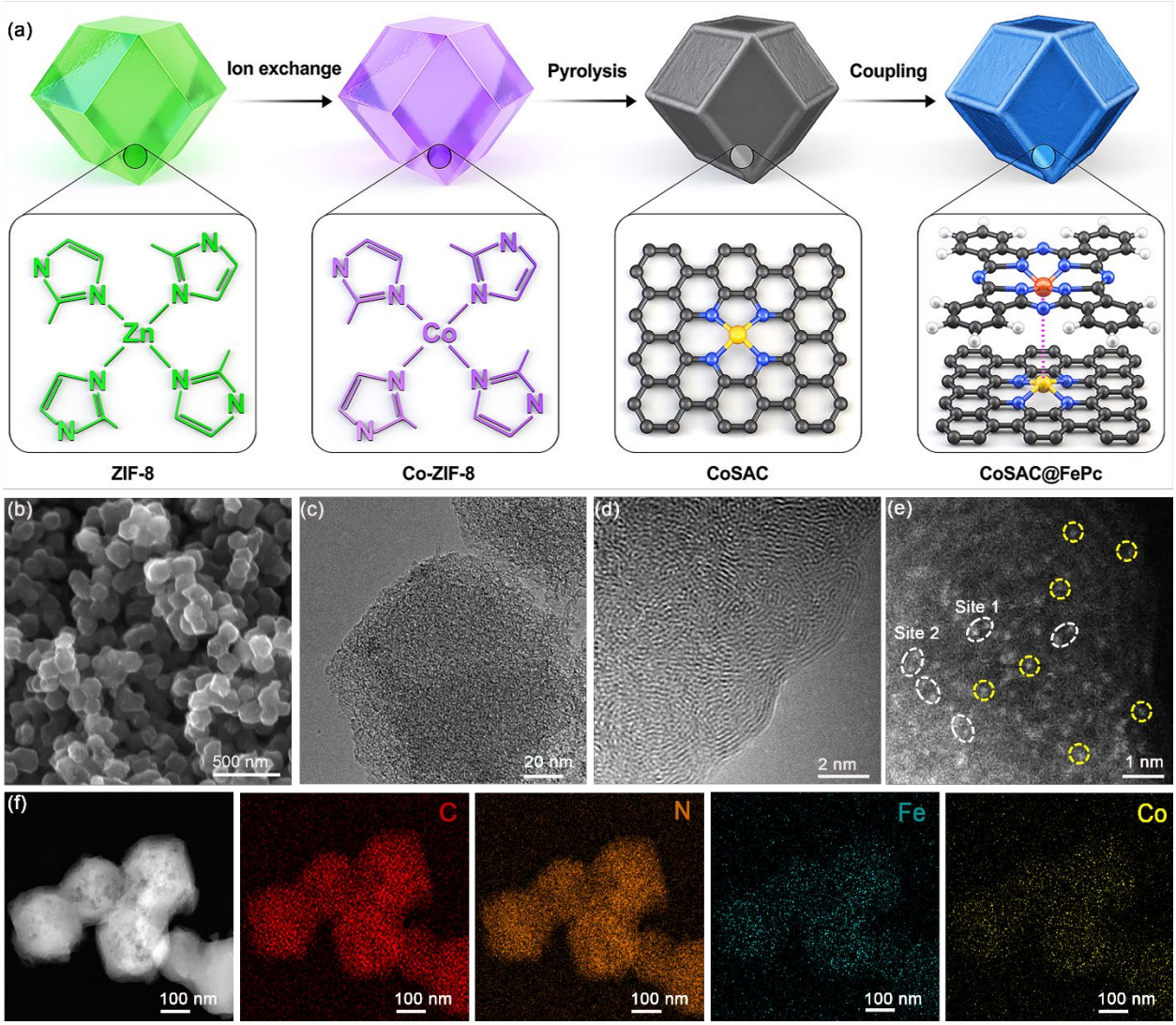

Figure 1. Synthesis scheme and morphology characterization of CoSAC@FePc. a) Schematic illustration for the synthetic process of CoSAC@FePc. b) SEM, c, d) TEM, and e) HAADF-STEM images of CoSAC@FePc(yellow circle mean Co atom/Fe atom and white circle mean paired Co−Fe atoms). F) TEM image and corresponding elemental of CoSAC@FePc.

TEM imaging was employed to further reveal the structural details of CoSAC@FePc. Porous polyhedral nanoparticles are present in CoSAC@FePc (Figure S5, Supporting Information), which

is similar to that of CoSAC (Figure S6, Supporting Information). No metal nanoparticle was observed during the TEM characterization process. Figure 1c shows a high-resolution TEM image of CoSAC@FePc. Nanopores composed of distorted graphite layers are present in CoSAC@FePc (Figure 1d), which suggests its good electrical conductivity and potential catalytic benefits.[24] The pore structure of CoSAC@FePc was further evaluated by N_2 adsorption and desorption test. Abundant nanopores are present in CoSAC@FePc, and its Brunauer–Emmett–Teller surface area reaches as high as 782 $m^2 g^{-1}$ (Figure S7, Supporting Information). To further reveal the structural information at the atomic level, we carried out aberration-corrected high-angle annular dark-field scanning TEM (HAADF-STEM) imaging. Dense bright spots are observed on the surface of polyhedral CoSAC@FePc nanoparticles (Figure S8, Supporting Information). Such bright spots should be attributed to isolated Co and/or Fe atoms. Higher magnification HAADF-STEM images show that two kinds of atomically dispersed metal species are present in CoSAC@FePc (Figure 1e). The first type is paired Co−Fe atoms marked by red circles, showing the distances of paired metal atoms are less than 2.64 Å (Figure S9, Supporting Information).[25] This value is determined through X-ray absorption spectroscopy analysis (discussed below) based on the face-to-face coupling interaction between Co-N_4 in CoSAC and Fe-N_4 in FePc. The other category is Fe and/or Co single atoms, indicated by yellow circles. Notably, one should consider that some overlapping bright spots might originate from the Co−Fe bond sites (indicated by red circles, designated as site 1 and site 2). Figure 1f shows the STEM imaging and corresponding Energy–dispersive X–ray spectroscopy (EDS) elemental mapping of CoSAC@FePc. Clearly, Co, Fe, C, and N evenly overlap on polyhedral nanoparticles, demonstrating that Co-N species coupled with FePc are successfully anchored on the polyhedral carbon nanoparticles.

2.2 Chemical state and Coordination analysis

X-ray photoelectron spectroscopy (XPS) analysis was performed to further understand the detailed elemental composition and chemical state on the surface of CoSAC@FePc. The atomic percentages of Co, Fe, N, and O are 0.19 at.%, 0.62 at.%, 7.73 at.%, and 7.62 at.% recorded from XPS surface analysis **(Figure 2**a and Figure S10a, Supporting Information), corresponding to the weight percentages of 0.87 wt.%, 2.71 wt.%, 8.44 wt.%, and 9.51 wt.%, respectively. Co and Fe contents were further measured by inductively coupled plasma mass spectrometry (ICP-MS), exhibiting only 0.67 wt.% of Fe and 0.03 wt.% of Co in CoSAC@FePc far below the values detected by XPS surface analysis. This result illustrates that most Co and Fe species are located on the surface of CoSAC@FePc.[26] High-resolution XPS Co 2p spectra display that six fitting peaks are present in CoSAC@FePc (Figure S10b, Supporting Information). Therein, 780.5 eV and 795.9 eV arise from Co^{2+}, while 785.2 eV and 801.8 eV correspond to Co^{3+}.[27] Likewise, the coexistence of Fe^{2+} and Fe^{3+} species is evident in CoSAC@FePc, as indicated by their binding energies (Figure S11, Supporting Information).[28] Figure S12 (Supporting Information) exhibits XPS N 1s spectra for CoSAC@FePc, along with control samples of CoSAC and NC@FePc. Pyridinic N, pyrrolic N, graphitic N and oxidized N are present in all three catalysts, i.e., CoSAC@FePc, CoSAC, and NC@FePc. Compared to CoSAC, CoSAC@FePc holds a relatively large negative shift of 1.92 eV because FePc anchored on the surface of CoSAC brings in large numbers of the low binding energy of N configurations, including pyridinic and pyrrolic N.

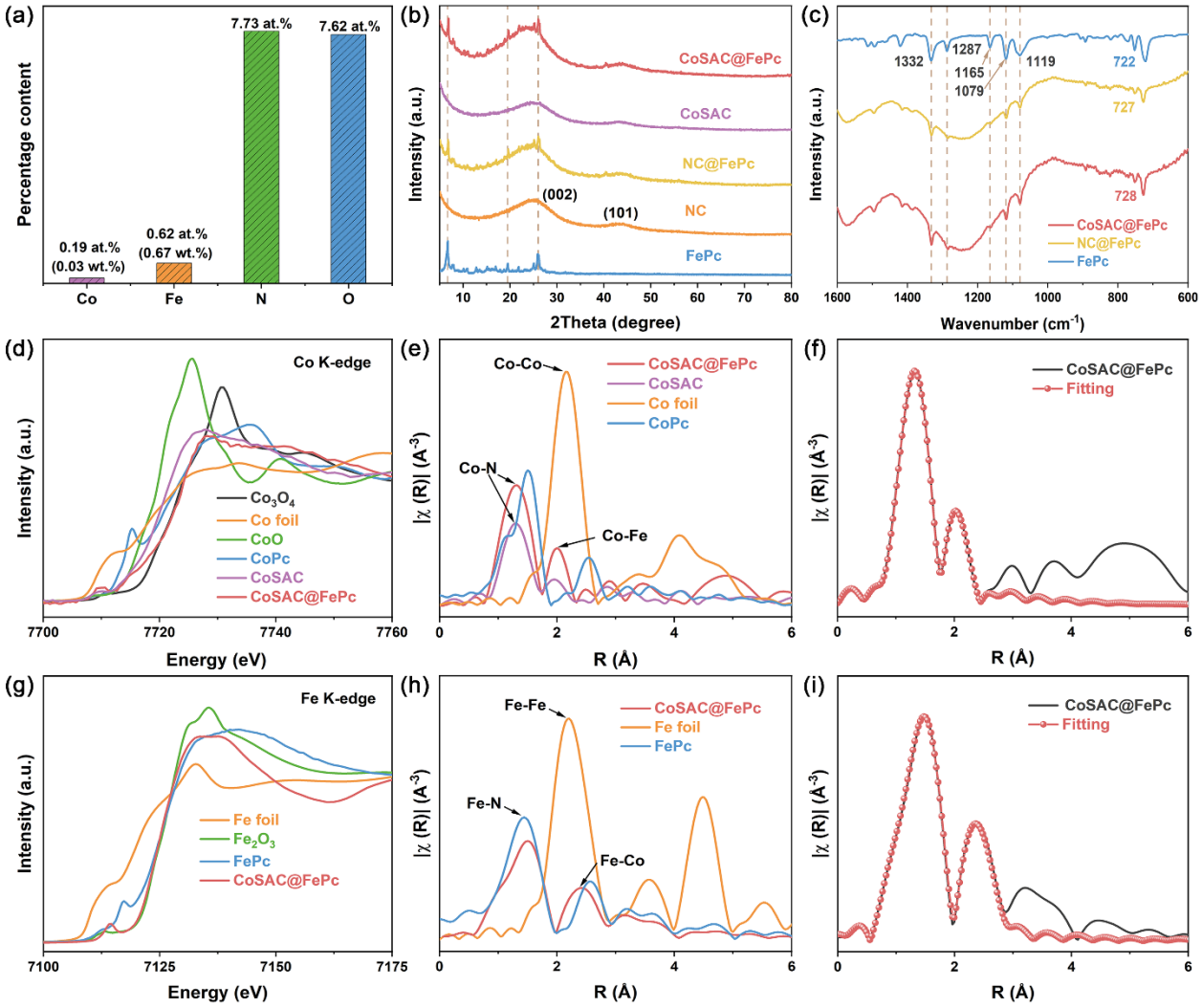

Figure 2. Structural analysis of the CoSAC@FePc and NC@FePc. a) Co, Fe, N, and O contents in CoSAC@FePc detected by XPS (at.%) and ICP-MS (wt.%) measurements. b) XRD patterns of CoSAC, CoSAC@FePc, NC, NC@FePc, and FePc. c) FT-IR spectra of CoSAC@FePc, NC@FePc, and FePc. d) Co and g) Fe K-edge XANES spectra of CoSAC@FePc and reference samples. e) Co and h) Fe K-edge FT-EXAFS spectra of CoSAC@FePc and reference samples. f) Co and i) Fe FT-EXAFS fitting curves of CoSAC@FePc.

X-ray diffraction (XRD) measurement and Fourier transform infrared (FT-IR) spectroscopy were further carried out to reveal the coupling interaction between CoSAC and FePc. As shown in Figure 2b, similar to NC@FePc, CoSAC@FePc have distinct XRD characteristic peaks mainly at 6.7°, 19.5° and 26.3° that originate from FePc species, indicating that FePc is existed. The slight peak shift in CoSAC@FePc might illustrate the occurrence of monomeric FePc attached to

CoSAC@FePc. Two broad characteristic peaks at about 25° and 43° can be attributed to the (002) and (101) planes of graphitized carbon.[27] Furthermore, no signal at 40.7° and 47.0° from Co-based nanocrystals was detected in the CoSAC and CoSAC@FePc samples, suggesting that Co can be in the form of single atoms.[33] The well-graphitized carbon structure of CoSAC@FePc was further demonstrated by its low D-band/G-band ratio in Raman spectra (Figure S13, Supporting Information), which favors the electrical conductivity of the catalysts.[34] Figure 2c shows the FTIR spectra of CoSAC@FePc, NC@FePc, and FePc. For the FePc reference, the characteristic peak at 722 cm^{-1} originates from the out-of-plane vibration of Fe-N, while the characteristic peaks at 1079 cm^{-1}, 1119 cm^{-1}, 1165 cm^{-1}, 1287 cm^{-1}, and 1332 cm^{-1} are attributable to the in-plane deformation of C-C, C-H, C-N, C=C and C=N. After coupling with carbon materials (CoSAC and NC), the first peak from the out-of-plane vibration shows an obvious blue shift (Figure S14, Supporting Information). This result indicates that strong interaction in the out-of-plane direction of FePc can be triggered by carbon substrate. As a result, the electronic structure of the $Fe-N_4$ active site undergoes reconstruction, leading to a reduction in the reaction energy barrier and an enhancement in ORR activity. Interestingly, in contrast to NC@FePc (with a blue shift value of 5 cm^{-1}), CoSAC@FePc exhibits a more significant blue shift (6 cm^{-1}). This indicates a stronger π–π coupling interaction, suggesting potentially improved ORR performance.

To reveal the configurations of coupling moieties in CoSAC@FePc, X-ray absorption spectroscopy measurements for CoSAC@FePc and control sample of CoSAC were carried out. The Co atoms exist as $Co-N_4$ species with a bond distance of 1.87 Å in CoSAC (Figure 2e, Figure S15 and Table S1, Supporting Information). Figure 2d exhibits the Co K-edge X-ray absorption near edge structure (XANES) spectra of CoSAC@FePc and normative reference samples of Co foil, CoO, cobalt phthalocyanine (CoPc), and Co_3O_4. The absorption edge of CoSAC@FePc lies

between CoO and Co_3O_4, which is similar to that of CoSAC (Figure 2d). This indicates that Co^{+2} and Co^{+3} are present in CoSAC@FePc, which is in good agreement with the XPS result. Fourier-transform extended X-ray absorption fine structure (FT-EXAFS) curves in Figure 2e show that the first-coordination-shell Co-N scattering peak of CoSAC@FePc (1.32 Å) undergoes a noticeable negative shift compared with CoPc (1.50 Å). This phenomenon is attributed to the typical effect of high-temperature pyrolysis, which usually tends to cause the contraction of Co-N bond.[29] Furthermore, a scattering peak at 2.01 Å, close to the first-coordination-shell Co-Co scattering peak of Co foil (2.17 Å) but smaller than the second-coordination-shell Co-C scattering peak of CoPc (2.54 Å), is present in CoSAC@FePc, which suggests the presence of Co-Fe bond in CoSAC@FePc.[30] Based on FT-EXAFS fitting result (Figure 2f and Table S2, Supporting Information), the coordination number is determined to be five, including planar Co-N_4 (Co-N bond: 1.86 Å) and axial Co-Fe (Co-Fe bond: 2.64 Å). A similar trend of Fe species in Fe K-edge XANES (Figure 2g) also illustrates the valence state (between +2 and +3) of Fe in CoSAC@FePc. Compared with FePc (7117 eV), the CoSAC@FePc has a lower first pre-edge peak (7114 eV), indicating that the symmetry of FePc in CoSAC@FePc can be broken due to the strong electronic interaction between FePc molecules and single Co atoms.[31] Figure 2h shows the Fe K-edge FT-EXAFS spectra of CoSAC@FePc, Fe foil, and FePc. The Fe-N scattering peak of CoSAC@FePc (1.50 Å) has a positive shift compared with FePc (1.44 Å), possibly due to the extension of the Fe-N bond. Besides, there also exists an obvious scattering peak at 2.42 Å in CoSAC@FePc, which locates between the first-coordination-shell Fe-Fe scattering peak of Fe foil (2.20 Å) and the second-coordination-shell Fe-C scattering peak of FePc (2.56 Å). This result illustrates Fe-Co bond can be present in CoSAC@FePc. According to the Fe K-edge FT-EXAFS fitting shown in Figure 2i and Table S2 (Supporting Information), the coordination number is five including planar

Fe-N_4 (Fe-N bond: 2.00 Å) and axial Fe-Co (Fe-Co bond: 2.66 Å). Notably, the Fe-N bond in CoSAC@FePc (2.00 Å) is longer than that in FePc (1.92 Å), which is due to the strong electron interaction between FePc and CoSAC as well as the coupling effect modulating the electronic structure of Fe-N_4. In addition, wavelet-transform (WT) analysis was performed to simultaneously reveal the local coordination environment in k and R spaces. The highest WT intensities of Co K-edge EXAFS at around 4.00 $Å^{-1}$ for both CoSAC@FePc and CoSAC are attributed to the Co-N bond, in contrast to that of Co foil (Figure S16, Supporting Information). The WT contour plots of Fe K-edge EXAFS reveal a noticeable positive shift in both k and R spaces for the Fe-N position (Figure S17, Supporting Information). This result further confirms the strong face-to-face coupling interaction between Fe-N_4 from FePc and Co-N_4 from CoSAC in CoSAC@FePc.

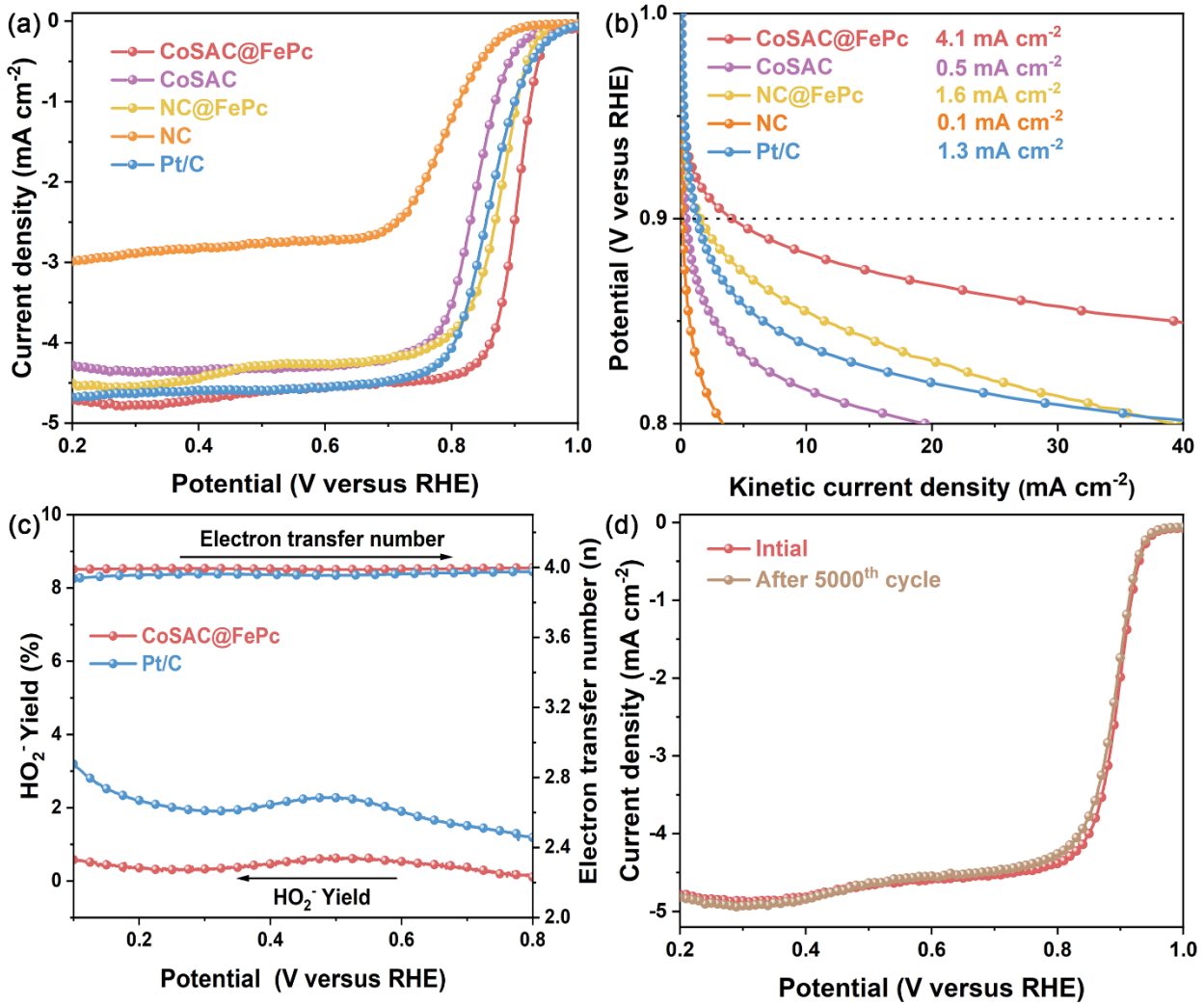

Figure 3. Electrocatalytic performance of CoSAC@FePc, CoSAC, NC@FePc, NC, Pt/C catalysts. a) LSV curves and b) the corresponding derived polarization curves of CoSAC@FePc, control samples, and commercial Pt/C catalyst recorded in 0.1 M KOH. c) Electron transfer number and HO_2^- yield of CoSAC@FePc and Pt/C derived from disk and ring currents. d) LSV polarization curves of CoSAC@FePc before and after 5000 CV potential cycles.

2.3 Electrochemical performance test and analysis

The ORR performance of CoSAC@FePc was measured using a rotating disk electrode (RDE) in 0.1 M KOH solutions. **Figure 3**a shows the linear sweep voltammetry (LSV) curves of CoSAC@FePc, CoSAC, NC@FePc, NC, and the Pt/C benchmark. Notably, CoSAC demonstrates remarkable ORR activity, exhibiting a half-wave potential ($E_{1/2}$) of 0.838 V, which surpasses that

of the metal-free NC catalyst ($E_{1/2}$=0.790 V) and aligns well with a previous report.[32] When FePc molecules were anchored on CoSAC and NC, the obtained hybrids substantially improved ORR activity, which demonstrates that Fe sites in the obtained hybrids dominate the ORR performance. The $E_{1/2}$ of CoSAC@FePc reaches as high as 0.904 V, surpassing those of Pt/C ($E_{1/2}$=0.860 V) and the majority of previously developed noble-metal-free catalysts (Table S3, Supporting Information). More interestingly, we observed substantial variation in ORR performance when using different carbon substrates (CoSAC and NC) to couple FePc molecules. NC@FePc, prepared by π–π coupling of FePc molecules and NC substrate, exhibits an $E_{1/2}$ of 0.876 V, which is lower than that of CoSAC@FePc. This result demonstrates that Fe-N_4 sites in FePc can interact with Co-N_4 sites in the CoSAC substrate, leading to the alteration of the electron structure of Fe active sites in CoSAC@FePc and resulting in an enhanced ORR activity. The kinetic current density curves of CoSAC@FePc, CoSAC, NC@FePc, NC, and Pt/C derived from mass transport correction are shown in Figure 3b. CoSAC@FePc exhibits a kinetic current density of 4.1 mA cm^{-2} at 0.9 V, which is 2.56 times higher than that of NC@FePc (1.6 mA cm^{-2}). The turn-over frequency of Fe sites in CoSAC@FePc is 1.77 e $site^{-1}$ s^{-1} at 0.9 V, 1.2 times as large as that of Fe sites in NC@FePc (1.45 e $site^{-1}$ s^{-1}). This further verifies that Co-N_4 sites can greatly enhance the ORR catalytic activity of Fe-active sites in FePc.

Figure 3c shows the HO_2^- by-product yields of CoSAC@FePc and Pt/C, derived from disk and ring currents of rotating ring-disk electrode measurements. At 0.1-0.8 V, CoSAC@FePc exhibits an HO_2^- yield of less than 0.7%, significantly outperforming that of Pt/C (below 3.2%). The remarkably low HO_2^- yield of CoSAC@FePc demonstrates its exceptional activity and selectivity for ORR. The average electron transfer number value of CoSAC@FePc is close to 4.0, indicating that it catalyzes the ORR following a thorough four-electron-transfer process. Besides,

the ORR stability of CoSAC@FePc, which is also a key factor for practical applications, was evaluated through cyclic voltammetry (CV) cycling measurement. As shown in Figure 3d, after 5000 potential cycles, the $E_{1/2}$ of CoSAC@FePc remains almost unchanged. In contrast, the commercial Pt/C catalyst shows a noticeable performance decay (Figure S18, Supporting Information). This result indicates superior ORR stability of CoSAC@FePc. Nevertheless, the ORR performance of CoSAC@FePc in acidic conditions is inferior to commercial Pt/C catalyst (Figure S19, Supporting Information).

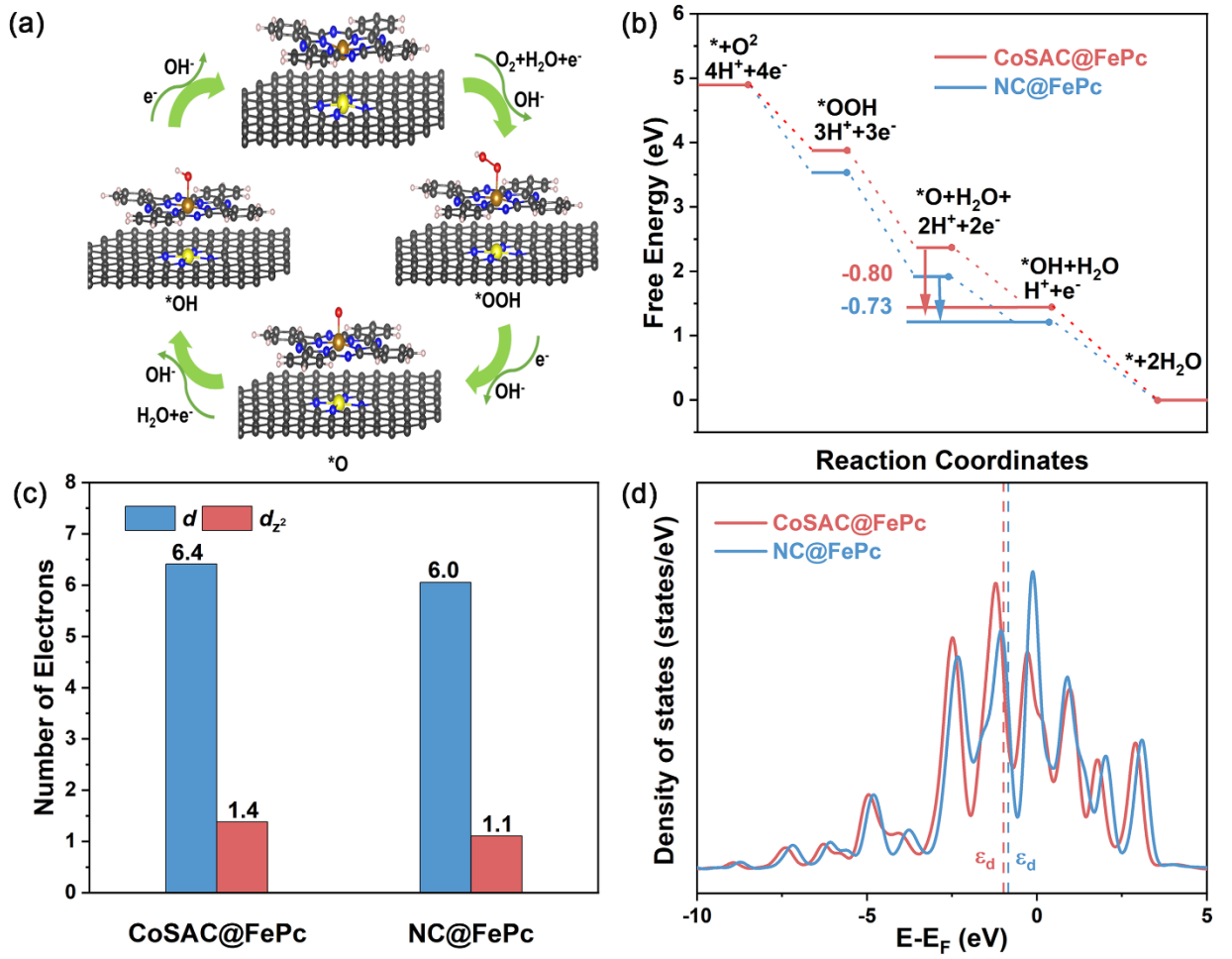

Figure 4. DFT calculations of CoSAC@FePc, NC@FePc catalysts. a) Schematic illustration of ORR process for the CoSAC@FePc model under alkaline conditions. The gray, blue, brown, yellow, red, and white balls represent the C, N, Fe, Co, O, and H atoms, respectively. b) Free energy diagrams of ORR processes on active

sites of the CoSAC@FePc and NC@FePc models at U = 0 V, pH = 13, and T = 298 K. c) Number of electrons filled in d and dz^2 orbitals of Fe atom in the CoSAC@FePc and NC@FePc models. d) Projected density of states of *d* orbital of Fe atom in the CoSAC@FePc and NC@FePc models.

2.4 Theoretical calculation and Mechanism analysis

To reveal the nature of the superior ORR performance of CoSAC@FePc, density functional theory (DFT) calculations were further conducted. A FePc molecule is coupled on Co-N_4 doped graphene support to construct the CoSAC@FePc model (Figure S20, Supporting Information), while a FePc molecule is anchored on pyridinic-N doped graphene support to model the NC@FePc structure (Figure S21, Supporting Information). The adsorption energy of FePc on CoSAC is -3.22 eV, which is stronger than that of FePc on Pyridinic-NC (-2.58 eV), indicating a stronger interaction between FePc molecule and Co-SAC support. The main oxygen-containing intermediates of *OOH, *O, and *OH are involved in the ORR, and the corresponding configurations of adsorption of intermediates on active sites of CoSAC@FePc and NC@FePc catalysts are shown in **Figure 4**a and Figure S22 (Supporting Information) respectively. Figure 4b shows the free energy diagrams of the ORR processes on active sites of the CoSAC@FePc and NC@FePc catalysts. It can be seen that, at the applied potential of $U = 0$ V, all the reaction steps are downhill in free energy for the ORR, implying facile reactions on these two catalysts. Besides, the least exergonic step, which is the rate-determining step, for both two catalysts is the reduction of *O to *OH, and therefore, the thermodynamic limiting potentials for CoSAC@FePc and NC@FePc catalysts are 0.80 and 0.73 V, respectively, corresponding to the theoretical overpotentials of 0.43 V for CoSAC@FePc and 0.50 V for NC@FePc. For the CoSAC model, the rate-determining step is the desorption of the *OH with the thermodynamic limiting potential of 0.60 eV, corresponding to the theoretical overpotentials of 0.63 V for CoSAC (Figure S23, Supporting Information). The lowest theoretical overpotential of ORR for CoSAC@FePc suggests

that CoSAC@FePc catalyst is energetically most favorable for the ORR process, which is well-aligned with our experimental results.

Furthermore, the charge density difference plotted in Figure S24 (Supporting Information) demonstrates that the charge transfer between Fe atom of FePc and Co atom of CoSAC is due to the strong electronic interaction between the FePc molecule and the CoSAC structure. This strong electronic interaction leads to the reconstruction of the electronic structure of Fe atom in FePc molecule. Compared to the Fe atom of FePc in the NC@FePc model, there are more electrons filled in the *d* orbital of Fe atom of FePc in the CoSAC@FePc model, as shown in Figure 4c. Particularly, more electrons are filled in the d_{z^2} orbital of Fe atom of FePc in the CoSAC@FePc model than that in the NC@FePc model, indicating the weaker binding strength between the active site and intermediates for the CoSAC@FePc model. This can be confirmed by the *d*-band center analysis. As Figure 4d shows that the *d*-band center of the Fe atom of FePc in the CoSAC@FePc model (-0.98 eV) is further with respect to the Fermi level than that in the NC@FePc model (-0.79 eV), indicating the weaker bonding interaction between the Fe atom and the intermediates for the CoSAC@FePc model, thus contributing to the superior ORR catalytic activity.

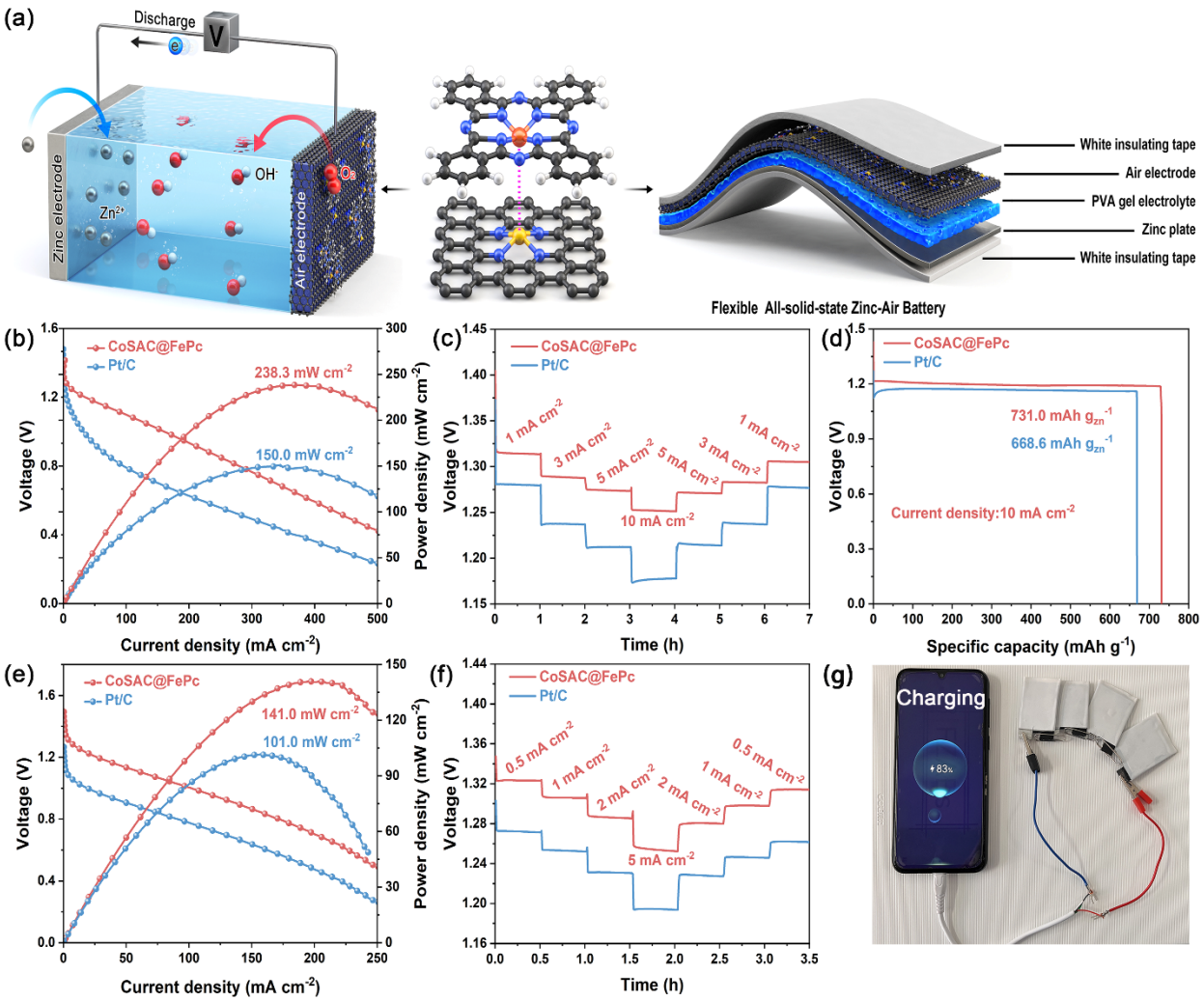

Figure 5. ZABs performance test. a) Models of Liquid-state and flexible soild-state Zn–air Batteries. b) Power density curves, c) rate performances, and d) specific capacities of liquid-state ZABs using CoSAC@FePc and Pt/C as the cathode catalysts. e) Power density curves and f) rate performances of solid-state ZABs based on CoSAC@FePc and Pt/C. g) Photograph of a mobile telephone powered by four flexible ZABs connected in series.

2.5 Zinc-Air Batteries (ZABs) performance test and analysis

Given the excellent ORR catalytic activity of CoSAC@FePc catalyst, we assembled liquid-state and flexible solid-state zinc-air batteries (ZABs) using CoSAC@FePc as the air cathode catalyst to evaluate its practical application. The diagrammatic drawing of ZABs can be seen in **Figure 5**a. For comparison, a commercial Pt/C catalyst was used as the benchmark for the ZAB. The open circuit potential (OCP) of liquid-state ZAB with CoSAC@FePc is 1.455 V (Figure S25,

Supporting Information), surpassing that of the ZAB with Pt/C (1.444 V), indicating its superior ORR activity. Figure 5b exhibits the ZAB polarization curves recorded at normal pressure and temperature in the air atmosphere. The CoSAC@FePc based ZAB exhibits a peak power density of 238.3 mW cm^{-2}, outperforming that of Pt/C (150.0 mW cm^{-2}). The rate performance was measured by constant-current discharging at different current densities. As shown in Figure 5c, the CoSAC@FePc cathode delivers significantly higher output voltages compared to that of Pt/C at the same discharge current densities ranging from 1 to 10 mA cm^{-2}, demonstrating its remarkable rate capability. Furthermore, specific capacity was evaluated according to Zn consumption during constant-current discharging. The specific capacity of CoSAC@FePc based ZAB reaches as high as 731.0 mAh g^{-1} at 10 mA cm^{-2} (Figure 5d), which far outperforms that of the Pt/C based ZAB (668.6 mAh g^{-1}). A comparison of ZAB performance between our CoSAC@FePc and advanced electrocatalysts is summarized in Table S4 (Supporting Information), highlighting that the ZAB based on CoSAC@FePc catalysts exhibits top-ranked battery performances.

Solid-state ZABs were further fabricated to investigate the practical application in flexible devices. CoSAC@FePc based solid-state ZAB displays an OCP of 1.327 V (Figure S26, Supporting Information). When this ZAB was treated with large bending angles of 90 º and 180º, its OCP remains almost unchanged. This result clearly highlights the remarkable suitability in flexible devices. Furthermore, the battery output performances including power density and rate capability were tested. Figure 5e displays that CoSAC@FePc based solid-state ZAB exhibits an impressive peak power density of 141.0 mW cm^{-2}, surpassing that of commercial Pt/C based reference ZAB (101.0 mW cm^{-2}). At the same discharge current densities, the CoSAC@FePc based cathode exhibits higher output voltages compared to that of the Pt/C based one (Figure 5f). The average discharge voltages are 1.323, 1.306, 1.286, and 1.254 V at 0.5, 1, 2, and 5 mA cm^{-2},

respectively. Upon the recovery of current density to 2, 1, and 0.5 mA cm^{-2}, the average discharge voltages (1.280 V, 1.298, and 1.314 V) nearly revert to their initial values. These results demonstrate excellent battery performance and promising application potential of the solid-state ZAB utilizing CoSAC@FePc. Furthermore, a performance comparison of solid-state ZABs based on CoSAC@FePc and advanced electrocatalysts demonstrates that the CoSAC@FePc cathode shows one of the best solid-state battery performances (Table S5, Supporting Information). Finally, four solid-state CoSAC@FePc based ZABs in series are used to power a telephone, shown in Figure 5g, which further verifies its good practicality.

3. Conclusion

A face-to-face laminated construction of Fe-N_4 and Co-N_4 in the hybrid catalyst of CoSAC@FePc is designed by FePc containing Fe-N_4 moieties coupling with Co-N_4 sites in single-atom catalyst of CoSAC. The Fe active centers in CoSAC@FePc coordinate with planar four N and axial Co, which is directly revealed by aberration-corrected HAADF-STEM imaging and X-ray absorption spectroscopy analysis. Such single-atom Co on the carbon substrate can modulate the electronic structure of FePc, leading to different out-of-plane vibrations of Fe-N, which is demonstrated by FTIR spectroscopy measurement. Theoretical calculations verify the Fe active centers in face-to-face Fe-N_4/Co-N_4 sites reduce the energy barrier of the rate-determining step for ORR, resulting in a low theoretical overpotential of 0.43 V and, therefore greatly boosting the ORR process. As a result, CoSAC@FePc exhibits outstanding ORR performance with a half-wave potential of 0.904 V, superior to commercial Pt/C and the overwhelming majority of electrocatalysts. The kinetic current density of CoSAC@FePc at 0.90 V is 2.56 times as large as that of the control sample of NC@FePc, in good agreement with theoretical calculations. Finally, CoSAC@FePc is used to

assemble liquid-state and solid-state ZABs, showing outstanding battery performances such as peak power densities of 238.3 mW cm^{-2} for liquid-state ZAB and 141.0 mW cm^{-2} for solid-state ZAB. Home-made battery demonstration including flexibility and mobile phone charging, verifies the excellent practicality of CoSAC@FePc based solid-state ZAB. This work develops a new single-metal-site catalyst by single-atom metal on the substrate to modulate the electronic structure and therefore boost the ORR, and promotes the development of metal-air batteries and fuel cells.

Supporting Information.

Material preparation, material characterization, electrochemical measurements, and computational methodology are available free of charge via the Internet at http://pubs.acs.org.

AUTHOR INFORMATION

Corresponding Author

*E-mail: shichao.ding@wsu.edu (S. Ding),

*E-mail: idkim@kaist.ac.kr (I. D. Kim)

*E-mail: jinchengli@kust.edu.cn (J. Li)

Author Contributions

The manuscript was written through contributions of all authors. All authors have given approval to the final version of the manuscript.

Notes

The authors declare no competing financial interest.

Acknowledgments

J.-C.L. would like to acknowledge the support by the National Natural Science Foundation of China (52102046), the Yunnan Fundamental Research Projects (202301AW070016), and the Applied Basic Research Program of Yunnan Province (Grant no. 202201AU070113).

TOC FIGURE

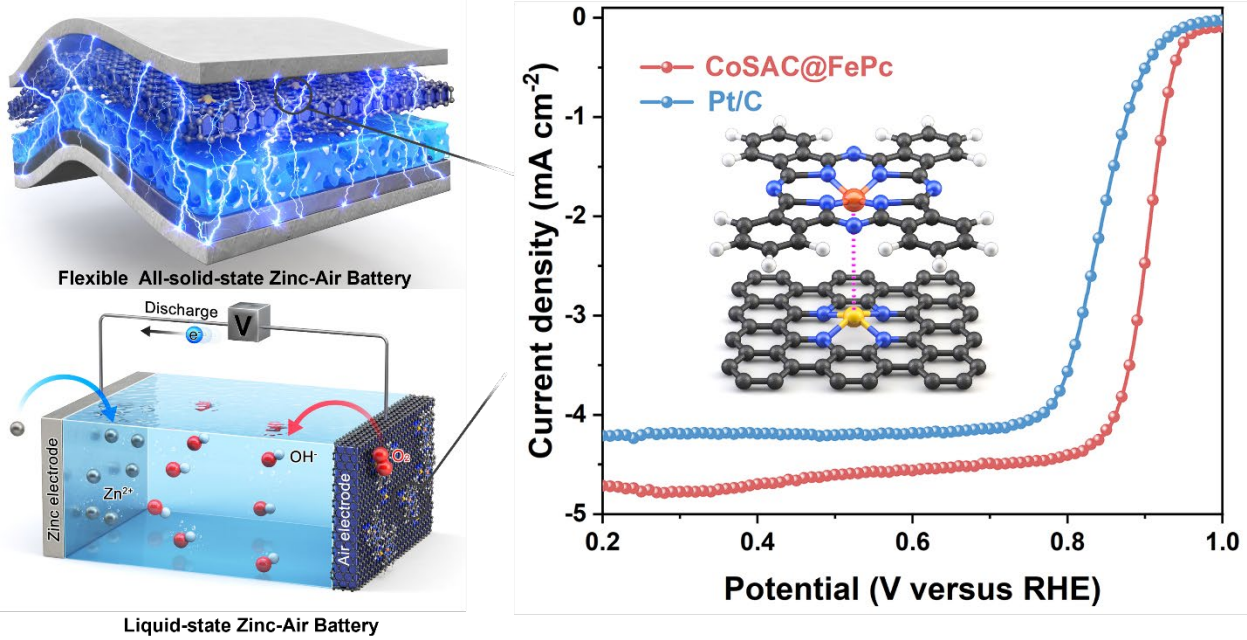

A new class of coupling hybrids that Me-N_4 macrocycle molecules anchored on carbon-based single-atom catalysts is developed to boost the catalytic activity for oxygen reduction reaction

Reference

[1] a) L. Yang, H. Liu, Z. Qiao, P. Sun, D. Li, R. Jiang, S. Liu, Z. Niu, Y. Zhang, T. Lin, Q. Zhang, L. Gu, S. Wang, D. Cao, Z. Chen, *Adv. Energy Mater.* **2023**, *13*, 2204390; b) X. Xiao, Z. Zheng, X. Zhong, R. Gao, Z. Piao, M. Jiao, G. Zhou, *ACS Nano* **2023**, *17*, 1764-1802; cC.-X. Zhao, J.-N. Liu, J. Wang, D. Ren, B.-Q. Li, Q. Zhang, *Chem. Soc. Rev.* **2021**, *50*, 7745-7778.

[2] S. S. A. Shah, T. Najam, M. S. Bashir, L. Peng, M. A. Nazir, M. S. Javed, *Energy Storage Mater.* **2022**, *45*, 301-322.

[3] S. Ding, J. A. Barr, Q. Shi, Y. Zeng, P. Tieu, Z. Lyu, L. Fang, T. Li, X. Pan, S. P. Beckman, D. Du, H. Lin, J.-C. Li, G. Wu, Y. Lin, *ACS Nano* **2022**, *16*, 15165-15174.

[4] a) J.-C. Li, P.-X. Hou, S.-Y. Zhao, C. Liu, D.-M. Tang, M. Cheng, F. Zhang, H.-M. Cheng, *Energy Environ. Sci.* **2016**, *9*, 3079-3084; b) C. Tang, L. Chen, H. Li, L. Li, Y. Jiao, Y. Zheng, H. Xu, K. Davey, S.-Z. Qiao, *J. Am. Chem. Soc.* **2021**, *143*, 7819-7827; c) X. Wan, X. Liu, Y. Li, R. Yu, L. Zheng, W. Yan, H. Wang, M. Xu, J. Shui, *Nat. Catal.* **2019**, *2*, 259-268.

[5] H. Zhang, S. Hwang, M. Wang, Z. Feng, S. Karakalos, L. Luo, Z. Qiao, X. Xie, C. Wang, D. Su, Y. Shao, G. Wu, *J. Am. Chem. Soc.* **2017**, *139*, 14143–14149.

[6] a) P. Zhu, X. Xiong, X. Wang, C. Ye, J. Li, W. Sun, X. Sun, J. Jiang, Z. Zhuang, D. Wang, Y. Li, *Nano Lett.* **2022**, *22*, 9507-9515; b) H.-B. Zhang, Y. Meng, H. Zhong, L. Zhang, S. Ding, L. Fang, T. Li, Y. Mei, P.-X. Hou, C. Liu, S. P. Beckman, Y. Lin, H.-M. Cheng, J.-C. Li, *Carbon Energy* **2023**, *5*, e289; c) L. Zong, K. Fan, P. Li, F. Lu, B. Li, L. Wang, *Adv.*

Energy Mater. **2023**, *13*, 2203611.
[7] a) H. Shang, X. Zhou, J. Dong, A. Li, X. Zhao, Q. Liu, Y. Lin, J. Pei, Z. Li, Z. Jiang, D. Zhou, L. Zheng, Y. Wang, J. Zhou, Z. Yang, R. Cao, R. Sarangi, T. Sun, X. Yang, X. Zheng, W. Yan, Z. Zhuang, J. Li, W. Chen, D. Wang, J. Zhang, Y. Li, *Nat. Commun.* **2020**, *11*, 3049; b) Q. Wei, X. Yang, G. Zhang, D. Wang, L. Zuin, D. Banham, L. Yang, S. Ye, Y. Wang, M. Mohamedi, S. Sun, *Appl. Catal., B* **2018**, *237*, 85-93; c) K. Yuan, S. Sfaelou, M. Qiu, D. Lützenkirchen-Hecht, X. Zhuang, Y. Chen, C. Yuan, X. Feng, U. Scherf, *ACS Energy Lett.* **2018**, *3*, 252-260.
[8] a) J. Zhang, H. Yang, B. Liu, *Adv. Energy Mater.* **2021**, *11*, 2002473; b) Y. He, S. Liu, C. Priest, Q. Shi, G. Wu, *Chem. Soc. Rev.* **2020**, *49*, 3484-3524; c) J.-C. Li, S. Maurya, Y. S. Kim, T. Li, L. Wang, Q. Shi, D. Liu, S. Feng, Y. Lin, M. Shao, *ACS Catal.* **2020**, *10*, 2452-2458.
[9] P. Cui, L. Zhao, Y. Long, L. Dai, C. Hu, *Angew. Chem. Int. Ed.* **2023**, *62*, e202218269.
[10] J.-C. Li, H. Zhong, M. Xu, T. Li, L. Wang, Q. Shi, S. Feng, Z. Lyu, D. Liu, D. Du, P. B. Scott, X. Pan, Y. Lin, M. Shao, *Sci. China Mater.* **2020**, *63*, 965-971.
[11] K. Yuan, D. Lützenkirchen-Hecht, L. Li, L. Shuai, Y. Li, R. Cao, M. Qiu, X. Zhuang, M. K. H. Leung, Y. Chen, U. Scherf, *J. Am. Chem. Soc.* **2020**, *142*, 2404–2412.
[12] a) H.-Y. Zhuo, X. Zhang, J.-X. Liang, Q. Yu, H. Xiao, J. Li, *Chem. Rev.* **2020**, *120*, 12315-12341; b) J.-C. Li, F. Xiao, H. Zhong, T. Li, M. Xu, L. Ma, M. Cheng, D. Liu, S. Feng, Q. Shi, H.-M. Cheng, C. Liu, D. Du, S. P. Beckman, X. Pan, Y. Lin, M. Shao, *ACS Catal.* **2019**, *9*, 5929-5934; c) J. Han, J. Bian, C. Sun, *Research* **2020**, *2020*, 9512763.
[13] a) H. Hu, Y. Meng, Y. Mei, P. X. Hou, C. Liu, H. M. Cheng, M. Shao, J. C. Li, *Energy Storage Mater.* **2023**, *54*, 517-523; b) Y. Wang, T. Zhou, S. Ruan, H. Feng, W. Bi, J. Hu, T. Chen, H. Liu, B. Yuan, N. Zhang, W. Wang, L. Zhang, W. Chu, C. Wu, Y. Xie, *Nano Lett.* **2022**, *22*, 6622–6630; c) S. Ding, L. He, L. Fang, Y. Zhu, T. Li, Z. Lyu, D. Du, Y. Lin, J.-C. Li, *Adv. Energy Mater.* **2022**, *12*, 2202984.
[14] a) S. Huang, D. Tranca, F. Rodríguez-Hernández, J. Zhang, C. Lu, J. Zhu, H. W. Liang, X. Zhuang, *Angew. Chem. Int. Ed.* **2023**, e202314833; b) B. Huang, S. Huang, C. Lu, L. Li, J. Chen, T. Hu, D. Lützenkirchen-Hecht, K. Yuan, X. Zhuang, Y. Chen, *CCS Chemistry* **2023**, *5,* 1876-1887.
[15] L. Li, X. Tang, S. Huang, C. Lu, D. Lützenkirchen-Hecht, K. Yuan, X. Zhuang, Y. Chen, *Angew. Chem. Int. Ed.* **2023**, *62,* e202301642
[16] X. Li, X. Wu, Y. Zhao, Y. Lin, J. Zhao, C. Wu, H. Liu, L. Shan, L. Yang, L. Song, J. Jiang, *Adv. Mater.* **2023***, 35,* 2302467.
[17] W. Wan, C. A. Triana, J. Lan, J. Li, C. S. Allen, Y. Zhao, M. Iannuzzi, G. R. Patzke, *ACS Nano* **2020**, *14*, 13279-13293.
[18] Y. Jiang, Y. Lu, X. Lv, D. Han, Q. Zhang, L. Niu, W. Chen, *ACS Catal.* **2013**, *3*, 1263-1271.
[19] K. Chen, K. Liu, P. An, H. Li, Y. Lin, J. Hu, C. Jia, J. Fu, H. Li, H. Liu, Z. Lin, W. Li, J. Li, Y.-R. Lu, T.-S. Chan, N. Zhang, M. Liu, *Nat. Commun.* **2020**, *11*, 4173.
[20] R. Cao, R. Thapa, H. Kim, X. Xu, M. Gyu Kim, Q. Li, N. Park, M. Liu, J. Cho, *Nat. Commun.* **2013**, *4*, 2076.
[21] X. Yu, S. Lai, S. Xin, S. Chen, X. Zhang, X. She, T. Zhan, X. Zhao, D. Yang, *Appl. Catal., B* **2021**, *280*, 119437.
[22] J. Yang, J. Tao, T. Isomura, H. Yanagi, I. Moriguchi, N. Nakashima, *Carbon* **2019**, *145*, 565-571.
[23] a) L. He, H. Hu, H.-B. Zhang, Y. Mei, J.-C. Li, *ACS Appl. Energy Mater.* **2022**, *5*, 14799-

14806; b) X. Huang, Y. Zhang, H. Shen, W. Li, T. Shen, Z. Ali, T. Tang, S. Guo, Q. Sun, Y. Hou, *ACS Energy Lett.* **2018**, *3*, 2914-2920; c) S. Feng, H. Zhong, J. Song, C. Zhu, P. Dong, Q. Shi, D. Liu, J. Li, Y.-C. Chang, S. P. Beckman, M.-k. Song, D. Du, Y. Lin, *ACS Appl. Energy Mater.* **2018**, *1*, 7014-7021.

[24] a) J.-C. Li, X. Qin, F. Xiao, C. Liang, M. Xu, Y. Meng, E. Sarnello, L. Fang, T. Li, S. Ding, Z. Lyu, S. Zhu, X. Pan, P.-X. Hou, C. Liu, Y. Lin, M. Shao, *Nano Lett.* **2021**, *21*, 4508-4515; b) S. Ding, Z. Lyu, L. Fang, T. Li, W. Zhu, S. Li, X. Li, J.-C. Li, D. Du, Y. Lin, *Small* **2021**, *17*, 2100664; c) S. Ding, Z. Lyu, E. Sarnello, M. Xu, L. Fang, H. Tian, S. E. Karcher, T. Li, X. Pan, J. McCloy, G. Ding, Q. Zhang, Q. Shi, D. Du, J.-C. Li, X. Zhang, Y. Lin, *J. Mater. Chem. A* **2022**, *10*, 5981-5989.

[25] a) C. Chen, M. Sun, F. Zhang, H. Li, M. Sun, P. Fang, T. Song, W. Chen, J. Dong, B. Rosen, P. Chen, B. Huang, Y. Li, *Energy Environ. Sci.* **2023**, *16*, 1685-1696; b) X. Zhou, J. Gao, Y. Hu, Z. Jin, K. Hu, K. M. Reddy, Q. Yuan, X. Lin, H.-J. Qiu, *Nano Lett.* **2022**, *22*, 3392-3399; c) Y. Wang, K. Li, R. Cheng, Q. Xue, F. Wang, Z. Yang, P. Meng, M. Jiang, J. Zhang, C. Fu, *Chem. Eng. J.* **2022**, *450*, 138213.

[26] D. Liu, J.-C. Li, S. Ding, Z. Lyu, S. Feng, H. Tian, C. Huyan, M. Xu, T. Li, D. Du, P. Liu, M. Shao, Y. Lin, *Small Methods* **2020**, *4*, 1900827.

[27] J.-C. Li, Y. Meng, L. Zhang, G. Li, Z. Shi, P.-X. Hou, C. Liu, H.-M. Cheng, M. Shao, *Adv. Funct. Mater.* **2021**, *31*, 2103360.

[28] L. Zhu, H. Zhong, D. Du, T. Li, H. Nguyen, S. P. Beckman, W. Xu, J.-C. Li, N. Cheng, Y. Lin, *Nano Res.* **2023**, *16*, 5216-5225.

[29] X. X. Wang, D. A. Cullen, Y.-T. Pan, S. Hwang, M. Wang, Z. Feng, J. Wang, M. H. Engelhard, H. Zhang, Y. He, Y. Shao, D. Su, K. L. More, J. S. Spendelow, G. Wu, *Adv. Mater.* **2018**, *30*, 1706758

[30] J. Wang, W. Liu, G. Luo, Z. Li, C. Zhao, H. Zhang, M. Zhu, Q. Xu, X. Wang, C. Zhao, Y. Qu, Z. Yang, T. Yao, Y. Li, Y. Lin, Y. Wu, Y. Li, *Energy Environ. Sci.* **2018**, *11*, 3375-3379.

[31] W. Wan, C. A. Triana, J. Lan, J. Li, C. S. Allen, Y. Zhao, M. Iannuzzi, G. R. Patzke, *ACS Nano* **2020**, *14*, 13279-13293.

[32] X.-Q. Zhang, Z. Lyu, S. Ding, S. Zhao, G. Chen, Y. Lin, J.-C. Li, *J. Phys. Chem. C* **2023**, *127*, 11883-11890.

[33] X. Lyu, X. Gu, G. Li, H. Chen, H. Hou, J. Hu, *ChemCatChem* **2022**, *14*.

[34] D. Liu, J. C. Li, Q. Shi, S. Feng, Z. Lyu, S. Ding, L. Hao, Q. Zhang, C. Wang, M. Xu, T. Li, E. Sarnello, D. Du, Y. Lin, *ACS Appl Mater Interfaces* **2019**, *11*, 39820-39826.